On-chip silicon Mach–Zehnder interferometer sensor for ultrasound detection

Ouyang, Boling; Li, Yanlu; Kruidhof, Marten; Horsten, Roland; van Dongen, Koen W.A.; Caro, Jacob

DOI
10.1364/OL.44.001928

Publication date
2019

Document Version
Final published version

Published in
Optics Letters

Optics Letters

On-chip silicon Mach–Zehnder interferometer sensor for ultrasound detection

Boling Ouyang,[1,*] Yanlu Li,[2,3] Marten Kruidhof,[1] Roland Horsten,[1] Koen W. A. van Dongen,[1] and Jacob Caro[1]

[1]Department of Imaging Physics, Delft University of Technology, Lorentzweg 1, 2628 CJ Delft, The Netherlands
[2]Photonics Research Group, Ghent University-imec, Technologiepark-Zwijnaarde 126, 9052 Ghent, Belgium
[3]Center for Nano-and Biophotonics, Ghent University, Technologiepark-Zwijnaarde 126, 9052 Ghent, Belgium
*Corresponding author: B.Ouyang@tudelft.nl

Received 11 February 2019; accepted 2 March 2019; posted 7 March 2019 (Doc. ID 358583); published 4 April 2019

A highly sensitive ultrasound sensor based on an integrated photonics Mach–Zehnder interferometer (MZI) fabricated in silicon-on-insulator technology is reported. The sensing spiral is located on a membrane of size 121 μm × 121 μm. Ultrasound waves excite the membrane's vibrational mode, which translates to modulation of the MZI transmission. The measured sensor transfer function is centered at 0.47 MHz and has a −6 dB bandwidth of 21.2%. The sensor sensitivity is linear in the optical input power and reaches a maximum 0.62 mV/Pa, which is limited by the interrogation method. At 0.47 MHz and for an optical power of 1.0 mW the detection limit is 0.38 mPa/Hz$^{1/2}$ and the dynamic range is 59 dB. The MZI's gradual transmission function allows a wide range of wavelength operation points. This strongly facilitates sensor use and is promising for applications.

https://doi.org/10.1364/OL.44.001928

Integrated photonics, an enabling technology for many application fields, has widely pervaded photonic sensing [1,2], with applications in environmental, chemical, and biomedical sensing. An important advantage of integrated photonic sensors is their small size, mass producibility, low cost, and electromagnetic immunity. Ring resonators (RRs) and Mach–Zehnder interferometers (MZIs) are very sensitive sensors in various contexts [1,2] and have a simple waveguide architecture. The sensor signal of these devices results from a refractive index change of the waveguide section responding to the agent to be sensed. For RR sensors, the signal is a shift of the well-separated and sharp resonance peaks, while for the MZIs it is a shift of the continuous sinusoidal transmission spectrum. The MZI goes back to the pioneering work of Zehnder [3] and Mach [4] on free space optics interferometers, that can be used for sensing of macroscopic samples. Integrated photonics versions of MZIs have also been realized in photonic crystals, using self-collimation of light [5], where the ratio of the two MZI outputs is the sensing signal.

Recently, RRs made in polymer and silicon-on-insulator (SOI) platforms have been used to sense ultrasound [6–9]. For the polymer RRs, located on a rigid substrate, the optoelastic effect leads to ultrasound induced resonance-wavelength modulation. In [6] a polymer RR sensor is demonstrated for ultrasound in the range 1–75 MHz, giving a lowest measurable pressure (noise equivalent pressure, NEP) of 10.5 Pa. Polymers with a higher refractive index are suggested for bending radii below 20 μm. In [7] an all-optical photoacoustic imaging is presented using a polymer RR sensor. The RR sensor in SOI [8,9] developed at our department is located on a membrane sensitive to ultrasound waves, such that periodic membrane deflection at the ultrasound frequency leads to the sensor signal via transduction to the RR. This sensor has a high sensitivity owing to a high quality factor and a NEP as small as 0.4 Pa. Interrogating the sensor requires some care in view of the limited predictability of the quality factor and the resonance wavelengths due to inherent variability of the fabrication and nonlinear effects already occurring at moderate optical power, leading to bistability of the resonances [10].

An MZI sensor for static gas pressures, also based on the membrane principle, is reported in [11]. An MZI optical microphone is demonstrated in [12] for acoustic waves in air up to 20 kHz, i.e., limited to frequencies of human hearing. For waveguides fabricated in SOI, on a rigid substrate and inserted in the arms of a fiber-based MZI, the effect of polarization and waveguide dimensions on the sensitivity of ultrasound detection is analyzed in [13].

In this Letter, we present a robust on-chip MZI sensor for ultrasound, fabricated in CMOS compatible SOI technology. The sensing spiral of the MZI is located on a square SiO_2 membrane, designed to mechanically resonate at MHz frequencies in water. With our MZI sensor we achieve considerable extension of the frequency-operation range compared to the ranges in [11,12], in particular reaching frequencies for ultrasound imaging. An MZI does not exhibit nonlinear effects up to relatively high optical power, which is helpful for the sensitivity. As for interrogating the sensor, it is very advantageous that its transmission characteristic is gradual, instead of sharp as it is for a RR. This allows a wide wavelength-operation range, facilitating sensor use and making it robust.

Figure 1(a) shows a schematic of the MZI sensor. Laser light of telecom wavelengths is guided towards two spiral-shaped

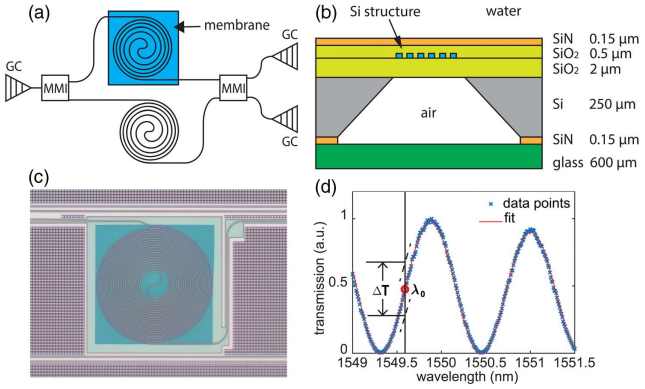

Fig. 1. (a) Schematic of the MZI ultrasound sensor. (b) Cross-section of the membrane region. A glass platelet seals the air cavity under the membrane. (c) Microscope image of the sensing region, showing the spiral on the membrane. Membrane diameter is 121 µm × 121 µm. The dense non-photonic structures outside the membrane are the so-called tiling. (d) Normalized transmission spectrum of the MZI sensor. The transmission includes the effect of the grating coupler, which explains the decreasing amplitude with increasing wavelength. At operation wavelength λ_0 the peak-to-peak transmission modulation ΔT resulting from an ultrasound pulse is indicated.

waveguide arms of different length via a 50:50 multi-mode interferometer (MMI), using an input grating coupler (GC). The light leaving the arms is combined in 2 × 2 MMI and coupled out by two other GCs. The sensing arm is located on a square membrane, acting as a mechanical resonator with a resonance frequency in the MHz range. The reference arm is on the intact substrate.

MZIs as in Fig. 1(a) were fabricated at IMEC through the Europractice MPW service on a CMOS compatible SOI platform [220 nm Si layer, 2 µm buried oxide (BOX)]. The waveguides of the MZI arms are 450 nm wide. Sensors result after post-processing steps. The first step is thinning down the wafer to 250 µm. After dicing, a 0.5 µm thick SiO_2 layer is deposited as waveguide cladding by plasma-enhanced chemical vapor deposition on the chip level. Then, by low pressure chemical vapor deposition on both chip sides a 0.15 µm thick Si_3N_4 layer is deposited, to act as mask in the etch to follow. On the backside, a square centered at the sensing spirals is opened in the Si_3N_4 layer, using optical lithography and reactive ion etching in a fluorine based plasma. Then, a membrane of total thickness of 2.65 µm is created under the spiral by locally removing the Si substrate in a KOH etch, using the BOX layer as etch stop. This crystallographic etch yields the typical truncated pyramidal hole shown in Fig. 1(b). The size of the square opened in the Si_3N_4 mask gives accurate control of the membrane size, which in the present case is 121 µm × 121 µm. In packaging, the chip is glued on a glass platelet. Thus, in water the membrane is water loaded on one side and air loaded on the other side. To couple light into and out of the chip in water, fibers with a reflective coating on a polished angled facet are glued on the input and output GCs using UV curable glue. A schematic cross-section of the membrane region and a microscope image of the sensor are presented in Fig. 1(b) and 1(c), respectively. As can be seen in Fig. 1(c), the membrane is accurately aligned to the spiral. The membrane size is controlled to just cover the spiral. The length of the spiral is 4.5 mm, making the MZI very sensitive for sensing ultrasound waves.

The operation of the MZI sensor is of optomechanical nature. Ultrasound waves of proper characteristics incident on the membrane excite its vibrational mode, giving time-periodic strain of the spiral waveguide according to the profile and amplitude of the mode. This leads to modulation of the spiral length and, due to the optoelastic effect, of the effective index of the spiral waveguide. These, in turn, translate to phase modulation of the guided mode arriving at the combiner MMI and thus to a modulation of the MZI output power at constant operation wavelength λ_0. The amplitude of the phase modulation of the arriving mode is

$$\Delta\varphi(\lambda_0, L_s, L_s^*) = \frac{2\pi}{\lambda_0}\left(\int_{L_s^*} n_e^*(\lambda_0, l)\mathrm{d}l - \int_{L_s} n_e(\lambda_0, l)\mathrm{d}l\right), \quad \textbf{(1)}$$

where n_e (n_e^*) and L_s (L_s^*) are the effective index and length of the spiral on the strainless (maximally strained) membrane.

The MZI sensor is first characterized from its optical transmission without applied ultrasound, by sweeping the wavelength of a tunable laser (Santec, TSL-210, step size 10 pm) coupled to its input and by measuring the output power with a photodetector (Newport, 1811-FC-AC). A resulting spectrum is shown in Fig. 1(d), normalized to its maximum. The spectrum properly shows the expected oscillations, while the smaller amplitude at 1551 nm results from the GC transmission. We fit the following function to the normalized measured transmission

$$T(\lambda) = (a\lambda + b)\left[\frac{1}{2}\cos\left(2\pi\frac{\lambda}{\mathrm{FSR}} + \Phi(t)\right) + \frac{1}{2}\right], \quad \textbf{(2)}$$

where the factor in square brackets is the MZI transmission and $(a\lambda + b)$ is the first order approximation of the GC transmission in the relevant range. λ is the wavelength and FSR is the MZI free spectral range. The time dependence of the phase $\Phi(t)$ applies when ultrasound waves induce a modulation term, as a result of the phase modulation related to Eq. (1). The fit, also shown in Fig. 1(d), gives FSR = 1.13 nm, corresponding to an OPD of 2.13 mm.

The sensing properties of the sensor are determined with the setup shown in Fig. 2(a). The sensor and a piezo-transducer (Olympus, V318-SU) are coaxially mounted 230 mm apart on the opposite sides of a U-shaped frame, which is submerged in a water tank. The ultrasound waves impinge perpendicularly upon the membrane. An arbitrary waveform generator (Agilent, 33521A) applies Gaussian modulated sinusoidal voltage pulses to the transducer to obtain acoustic pressure pulses in the time domain given by

$$p(t) = p_0 \exp\left[-\left(\frac{t - \tau_d}{N/(2f_0)}\right)^2\right]\sin(2\pi f_0 t). \quad \textbf{(3)}$$

Here p_0, τ_d, and f_0 are the pressure amplitude, delay time, and center frequency of the pulse, respectively, and N is about half the number of cycles in the envelope. N determines the frequency bandwidth of the pulse. We choose $N = 10$, to have a narrow bandwidth pulse. The sensor is actuated by the tunable laser set at an operation wavelength and a constant power, also aligning the polarization with a polarization controller (Thorlabs, FPC562) for maximum GC transmission. The average optical power transmitted by the MZI is monitored at the

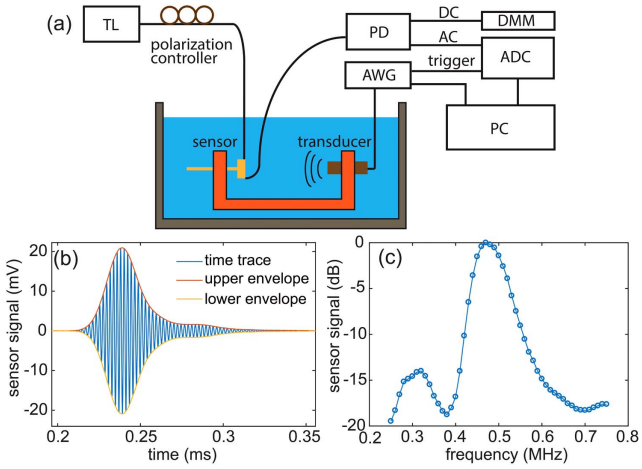

Fig. 2. (a) Schematic of the experimental setup for characterizing the MZI sensor (TL, tunable laser; PD, photodetector; AWG, arbitrary waveform generator; DMM, digital multimeter; ADC, analog-to-digital converter). (b) Time response of the sensor to a Gaussian ultrasound pulse centered at 0.47 MHz, for a maximum sensitivity operation wavelength discussed in the text related to Eq. (4). (c) Normalized transfer function of the sensor, obtained with an input power of 1.0 mW.

DC output of the photodetector to keep track of effects due to environmental temperature drift. The resulting wavelength drift of transmission curves as in Fig. 1(d) is found within ≈10 pm in the experiments reported below. The photodetector's AC output, representing the sensor response to incident acoustic pulses, is recorded by a 14-bit analog-to-digital converter (ADC, Spectrum, M3i4142-exp).

A typical time response of the sensor to a pulse given by Eq. (3) is shown in Fig. 2(b), for $p_0 = 32.2$ Pa, an input power of 1.0 mW and $f_0 = 0.47$ MHz (the membrane's resonance frequency; see below). The response closely mimics the Gaussian excitation pulse, with the addition of a tail, due to ringing down of the resonance.

To obtain the sensor transfer function, i.e., the sensor signal as a function of frequency f at constant amplitude p_0, time responses as in Fig. 2(b) are measured by sweeping f_0 from 0.25 to 0.75 MHz with 0.01 MHz step size. At each frequency the actual response is obtained as an average of 500 individual responses. The maximum of the signal envelop [see Fig. 2(b)], calculated from the Hilbert transform of the response, is taken as the sensor signal. We correct for the transducer's frequency characteristic, measured using a hydrophone (Precision Acoustics, 1 mm). In Fig. 2(c) we present the resulting normalized transfer function, which shows two resonance line shapes. The dominant resonance has its maximum at 0.47 MHz and corresponds to the membrane's lowest vibrational mode. We speculate that the much weaker sub-resonance at 0.32 MHz arises from a mode related to perturbation of the bare membrane by the dense spiral.

The sensitivity of the sensor at the transfer-function maximum of 0.47 MHz is the next function to determine. We define the wavelength dependent sensitivity as

$$S(\lambda) = \alpha I_{\text{in}} \left| \frac{dT}{dp} \right| = \alpha I_{\text{in}} \left| \frac{dT}{d\lambda} \frac{d\lambda}{dp} \right| \approx \alpha I_{\text{in}} \left| \frac{dT}{d\varphi} \frac{\Delta\varphi}{\Delta p} \right|, \quad (4)$$

where α represents the overall loss and gain, I_{in} is the optical input power, and p is the incident ultrasound pressure. $\Delta\varphi$ is given by Eq. (1). Δp is the change with respect to zero pressure and, thus, equals p. For small p, the response is expected linear, and both $d\lambda/dp$ and $\Delta\varphi/\Delta p$ are constant. Thus, at contact pressure the sensitivity is proportional to I_{in} and to $|dT/d\lambda|$. The time response in Fig. 2(b) is for operational wavelength $\lambda_0 = 1549.59$ nm [indicated in Fig. 1(d)], where $|dT/d\lambda|$ and, thus, the sensitivity are maximum.

The sensitivity is obtained by first measuring the time response for 33 pressure amplitudes of the Gaussian pulse in the range 0.77–341 Pa (maximum pressure 341 Pa limited by voltage range of ADC card, not by the sensor itself; amplitudes calibrated with the hydrophone) and this for 6 optical powers up to 1.0 mW actuating the sensor. The sensor's averaged time response is bandpass filtered (0.1–1.1 MHz, Tukey window) for noise reduction outside the range of interest. The results, presented in Fig. 3(a), along with fitted straight lines, clearly show linear behavior of the signal amplitude (i.e., maximum of envelope of time response) versus pressure down to the lowest pressure. This confirms that we indeed are working in the linear response regime. A high degree of linearity is also seen in the plot of the sensitivity versus optical input power in Fig. 3(b), where according to Eq. (4) plotted sensitivity values equal the slopes of the lines in Fig. 3(a). The sensitivity ranges from 0.31 to 0.62 mV/Pa. As a result of these high values, we can measure acoustic pressures down to 0.77 Pa with a high resolution.

The lowest measurable acoustic pressure or NEP, is obtained as the root-mean-square (RMS) noise divided by the sensitivity. To obtain the dependence of the NEP on optical power, we record time traces of the photodetector output for 0.5 ms after each data set of Fig. 3(a) for a specific power, without applying ultrasound and averaging, but with using the bandpass filter. 0.5 ms is the same measuring period as used for a single time response contributing to data points in Fig. 3(a). Thus, noise traces are taken under the conditions of the acoustic measurements. As shown in Fig. 3(c), the RMS noise increases from 0.194 to 0.237 mV in the range of applied powers. This behavior mainly results from increasing amplification of the intrinsic sensor noise with increasing power. The noise increase is weaker than the sensitivity increase, causing a

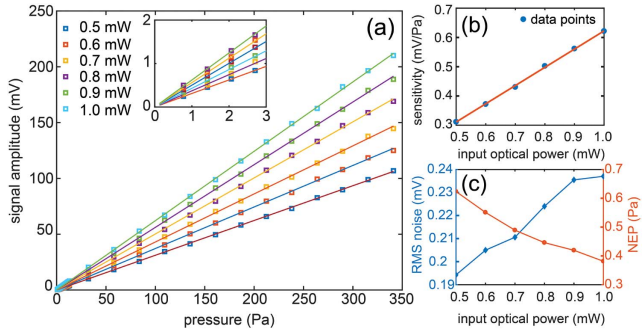

Fig. 3. (a) Sensor–signal amplitude as a function of the amplitude of the acoustic pressure pulse, for different optical input powers. The lines are linear fits to the data points. Inset: zoom-in of the low pressure range. (b) Sensor sensitivity as a function of optical input power. Again, the line is a linear fit. (c) Root-mean-square noise (blue) and noise equivalent pressure (red) as a function of optical input power.

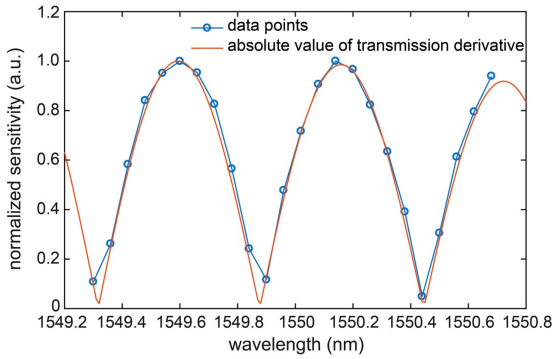

Fig. 4. Wavelength dependence of the sensor sensitivity. The data points agree excellently with the prediction given by Eq. (4).

notable NEP decrease with increasing power [see Fig. 3(c)]. For an input power of 1.0 mW, the NEP is 0.38 Pa, corresponding to a detection limit of 0.38 mPa/Hz$^{1/2}$.

As a final experiment, we test the prediction of the wavelength dependence of the sensitivity in Eq. (4). We follow the same procedure as used for acquiring the sensitivities in Fig. 3(b). Operation wavelengths are in the range 1549.30–1550.68 nm, with a 0.06 nm increment, thus covering one FSR of the MZI transmission. The optical input power is 1.0 mW. The results are plotted in Fig. 4 as normalized sensitivity, along with the absolute value of the derivative of the fitted transmission curve in Fig. 1(d). Excellent agreement of experiment and prediction is observed. The sensor is robust with respect to possible wavelength misalignment to a maximum sensitivity point, as this can be compensated by simply increasing the optical power without inducing nonlinear effects (see below). The wide FWHM of the sensitivity branches (≈400 pm), compared to a FWHM ≈ 100 pm for Si RR sensors [8,9] is of additional help here.

Having reported the experimental results, we now discuss several remaining aspects.

As for the transfer function, specific applications, e.g., photoacoustic imaging [14], may require its frequencies at several MHz and a larger bandwidth. This can be realized with modified membrane designs. The membrane-resonance frequency scales with h/d^2 [15], where h and d are the thickness and side of the square membrane, respectively. A frequency increase of 10 times thus can be easily achieved. To increase the bandwidth, the membrane can be made lossy by depositing a polymer layer on it. These adaptations go at the cost of sensitivity, which can be compensated by increasing the optical power.

The sensitivity of the sensor can be increased as follows. A first way is creating a stronger strain response to pressure. This also involves membrane redesign, now a thinner and larger membrane, which counteracts possible requirements for the transfer function. A larger membrane also offers a second way, namely a longer spiral, which adds to the sensitivity via $\Delta\varphi$ [see Eq. (1)]. Finally, one can simply increase the optical power, as suggested by Eq. (4) and Fig. 3(b). With an MZI not being a resonator, unlike a RR, there is no field enhancement. Thus, higher powers may be applied to the MZI without showing nonlinear effects. The maximum optical input power of 1.0 mW used here will already induce nonlinear effects in a Si RR sensor [10].

Combining the minimum NEP of 0.38 Pa and the maximum pressure of 341 Pa yields a dynamic range of 59 dB, which is appreciable. The trend for the NEP in Fig. 3(c) and the option to strongly increase the optical power indicate that the NEP can be further decreased and the dynamic range further increased. In addition, it is possible to use higher pressures than 341 Pa.

In conclusion, we demonstrate an on-chip MZI ultrasound sensor, fabricated in SOI technology. The sensing spiral is located on a 121 μm × 121 μm membrane, of which the mechanical resonance is excited by ultrasound waves around 0.47 MHz. The mechanical vibrations induce optical transmission modulation, thus defining the sensor signal. As the MZI transmission function is gradual, a wide wavelength-operation range is possible. We envision that a common distributed feedback laser as light source, the MZI sensor, and a photodetector can be integrated into a handheld single unit. The sensor transfer function, centered at 0.47 MHz, has a −6 dB bandwidth of 21.2%. We reach a maximum sensitivity of 0.62 mV/Pa and a dynamic range of 59 dB. In our measurements, the detection limit is 0.38 mPa/Hz$^{1/2}$. We indicate how each sensor quality can be tailored and improved. Redesigning the membrane properties and increasing the optical power are important and readily attainable means for this. The combination of its merits make this on-chip MZI ultrasound sensor very promising for various applications, e.g., all-optical photoacoustic imaging.

Funding. Nederlandse Organisatie voor Wetenschappelijk Onderzoek (NWO) (13534).

Acknowledgment. The authors thank M. Haverdings and P. Kat for valuable discussions, L. Orbe and W. Bogaerts for help in photonics design, and U. Taskin for use of the ADC system. The Kavli Nanolab Delft is acknowledged for use of fabrication facilities and support.

REFERENCES

1. P. V. Lambeck, Meas. Sci. Technol. **17**, R93 (2006).
2. E. Luan, H. Shoman, D. M. Ratner, K. C. Cheung, and L. Chrostowski, Sensors **18**, 3519 (2018).
3. L. Zehnder, Z. Instrumentenkd. **11**, 275 (1891).
4. L. Mach, Z. Instrumentenkd. **12**, 89 (1892).
5. H. M. Nguyen, M. A. Dundar, R. W. van der Heijden, E. W. J. M. van der Drift, H. W. M. Salemink, S. Rogge, and J. Caro, Opt. Express **18**, 6437 (2010).
6. T. Ling, S.-L. Chen, and L. J. Guo, Appl. Phys. Lett. **98**, 204103 (2011).
7. B.-Y. Hsieh, S.-L. Chen, T. Ling, L. J. Guo, and P.-C. Li, Photoacoustics **2**, 39 (2014).
8. S. Leinders, W. Westerveld, J. Pozo, P. Van Neer, B. Snyder, P. O'Brien, H. Urbach, N. de Jong, and M. D. Verweij, Sci. Rep. **5**, 14328 (2015).
9. F. Grillo Peternella, B. Ouyang, R. Horsten, M. Haverdings, P. Kat, and J. Caro, Opt. Express **25**, 31622 (2017).
10. G. Priem, P. Dumon, W. Bogaerts, D. van Thourhout, G. Morthier, and R. Baets, Opt. Express **13**, 9623 (2005).
11. E. Hallynck and P. Bienstman, IEEE Photon. J. **4**, 443 (2012).
12. H. Gao, C. H. Huang, W. Westerveld, R. Haouari, B. Troia, F. Verhaegen, R. Jansen, B. Figeys, X. Rottenberg, and V. Rochus, in *19th International Conference on Thermal, Mechanical and Multi-Physics Simulation and Experiments in Microelectronics and Microsystems (EuroSimE)*, Toulouse, France, 2018, p. 1.
13. S. Tsesses, D. Aronovich, A. Grinberg, E. Hahamovich, and A. Rosenthal, Opt. Lett. **42**, 5262 (2017).
14. K. Jansen, A. F. W. van der Steen, H. M. M. van Beusekom, J. W. Oosterhuis, and G. van Soest, Opt. Lett. **36**, 597 (2011).
15. A. W. Leissa and M. S. Qatu, in *Vibrations of Continuous Systems* (McGraw-Hill, 2011), p. 230.